crystals

MDPI

Article

Analyses of Substrate-Dependent Broadband Microwave (1–40 GHz) Dielectric Properties of Pulsed Laser Deposited $Ba_{0.5}Sr_{0.5}TiO_3$ Films

Sandwip K. Dey [1], Sudheendran Kooriyattil [2], Shojan P. Pavunny [3,†], Ram S. Katiyar [3,*] and Guru Subramanyam [4]

[1] Materials Science and Engineering Program (SEMTE), Arizona State University, Tempe, AZ 85287-6106, USA; sandwip.dey@asu.edu
[2] Departments of Physics, Sree Kerala Varma College, Thrissur 680011, India; sudhi.kooriyattil@gmail.com
[3] Department of Physics, University of Puerto Rico, San Juan, PR 00925-2537, USA; shojanpp@gmail.com
[4] Center of Excellence for Thin-Film Research and Surface Engineering, University of Dayton, Dayton, OH 45469-0232, USA; gsubramanyam1@udayton.edu
† Current Address: Department of Electrical and Computer Engineering, University of Nebraska, Lincoln, NE 68588, USA.
* Correspondence: ram.katiyar@upr.edu

Abstract: $Ba_{0.5}Sr_{0.5}TiO_3$ (BST-0.5) thin films (600 nm) were deposited on single crystal MgO, $SrTiO_3$ (STO), and $LaAlO_3$ (LAO) substrates by pulsed laser deposition at an oxygen partial pressure of 80 mTorr and temperature of 720 °C. X-ray diffraction and in situ reflection high-energy electron diffraction routinely ascertained the epitaxial quality of the (100)-oriented nanocrystalline films. The broadband microwave (1–40 GHz) dielectric properties were measured using coplanar waveguide transmission line test structures. The out-of-plane relative permittivity ($\varepsilon_{\perp}^{/}$) exhibited strong substrate-dependent dielectric (relaxation) dispersions with their attendant peaks in loss tangent (tanδ), with the former dropping sharply from tens of thousands to ~1000 by 10 GHz. Although homogeneous in-plane strain ($\epsilon_{\parallel}$), enhances $\varepsilon_{\perp}^{/}$ with ${}^{BST-0.5}_{MgO}\varepsilon_{\perp}^{/} > {}^{BST-0.5}_{STO}\varepsilon_{\perp}^{/} > {}^{BST-0.5}_{LAO}\varepsilon_{\perp}^{/}$ at lower frequencies, two crossover points at 8.6 GHz and 18 GHz eventually change the trend to: ${}^{BST-0.5}_{STO}\varepsilon_{\perp}^{/} > {}^{BST-0.5}_{LAO}\varepsilon_{\perp}^{/} > {}^{BST-0.5}_{MgO}\varepsilon_{\perp}^{/}$. The dispersions are qualitatively interpreted using (a) theoretically calculated (T)–($\epsilon_{\parallel}$) phase diagram for single crystal and single domain BST-0.5 film, (b) theoretically predicted $\epsilon_{\parallel}$-dependent, $\varepsilon_{\perp}^{/}$ anomaly that does not account for frequency dependence, and (c) literature reports on intrinsic and extrinsic microstructural effects, including defects-induced inhomogeneous strain and strain gradients. From the Vendik and Zubko model, the defect parameter metric, ξ_s, was estimated to be 0.51 at 40 GHz for BST-0.5 film on STO.

Keywords: dielectric permittivity; loss tangent; epitaxial BST thin films; microwave characterization; homogeneous in-plane strain engineering; inhomogeneous strain

Citation: Dey, S.K.; Kooriyattil, S.; Pavunny, S.P.; Katiyar, R.S.; Subramanyam, G. Analyses of Substrate-Dependent Broadband Microwave (1–40 GHz) Dielectric Properties of Pulsed Laser Deposited $Ba_{0.5}Sr_{0.5}TiO_3$ Films. *Crystals* **2021**, *11*, 852. https://doi.org/10.3390/cryst11080852

Academic Editors: Marco Bazzan and Raghvendra Singh Yadav

Received: 28 April 2021
Accepted: 18 July 2021
Published: 22 July 2021

1. Introduction

As the demand for wireless data communication continues to grow, mutual interference of communication devices due to crowded electromagnetic (EM) spectrum currently available, limits many commercial and military applications. Effective utilization of EM spectrum requires advanced passive components that can be tuned electronically. To date, variable thin-film capacitors (varactors) based on voltage-tunable dielectrics, such as Barium Strontium Titanate ($Ba_xSr_{1-x}TiO_3$ or BST), are found to be attractive for microwave applications such as tunable filters, phase shifters, delay lines, and voltage-controlled oscillators [1–3]. For applications at room temperature, the two major compositions that are actively considered are $Ba_{0.5}Sr_{0.5}TiO_3$ (BST-0.5) and $Ba_{0.6}Sr_{0.4}TiO_3$ (BST-0.6) [4,5]. Note, a high relative dielectric permittivity of BST thin films on low-loss microwave substrates is

attractive for reducing the size of the capacitors, and other microwave components and circuits. In general, the maintenance of high dielectric permittivity and low loss tangent should result in higher dielectric tunability and lower quality factor (Q) at higher microwave frequencies.

Recently, homogeneous, and biaxial strain manipulation, also known as strain engineering, has been employed to engineer the properties of epitaxial single crystal films. In epitaxial perovskite films, where the strain and electrical polarization are coupled, phenomenological formalisms have been used to predict the appearance of unusual phases, phase transformations, and dielectric anomalies in single crystal and single domain films. The properties of homogeneous strain-dependent properties of various perovskite dielectric films and multilayers, including BST of various orientations, have been represented via temperature-strain phase diagrams and dielectric permittivity maps with no mention of any frequency dependences. To test the applicability of such concepts, and to enhance the relative permittivity of nanocrystalline but polydomain BST films, one may alter the degree of strain in the films by either varying the processing methods, substrate materials, deposition conditions, including the oxygen partial pressure (pO_2), and post-annealing treatments.

Here, a simple preliminary study is undertaken to observe any effects of the magnitude and sign (compressive versus tensile) of the in-plane strain, in nanocrystalline and epitaxial BST-0.5 thin films, on the broadband microwave (1–40 GHz) dielectric properties. The epi-BST-0.5 films, with a thickness of 600 nm, are deposited on lattice and thermal mismatched, non-ferroelectric oxide single crystal substrates, namely magnesium oxide (MgO), strontium titanate (STO), lanthanum oxide (LAO) by pulsed laser deposition (PLD) at a fixed pO_2, and temperature. The dispersions in the microwave permittivity and substrate (and thus strain) dependent trends are analyzed and qualitatively interpreted against the backdrop (briefly outlined in the background) of (a) results of density functional theory and theoretically calculated temperature-in-plane strain phase diagram and predicted strain-dependent dielectric permittivity anomaly in oriented, single crystal, and single domain BST-0.5 film, and (b) well-established and extensive literature reports on the intrinsic and extrinsic contributions and effects on the dielectric responses.

2. Background

2.1. Intrinsic and Extrinsic Contributions to Dielectric Permittivity in Perovskites

To objectively assess the strain-mediated, microwave dielectric properties of BST-0.5 thin films, both intrinsic and extrinsic influences, underscored by Petzelt and coworkers [6–11], must be considered. These influences are functions of substrate type, growth conditions, and process-induced microstructure evolution. The intrinsic relative permittivity, ε_r, of cubic and centrosymmetric, perovskite-structured paraelectric oxides (e.g., STO and BST-0.5) stems from electronic and ionic polarizabilities; note, the latter arises from temperature-dependent transverse optical vibration mode, i.e., the soft mode, and other optically active lattice vibrations. The temperature dependence of ε_r above the critical Curie–Weiss temperature (T_o) can be described by the Curie–Weiss law, and the frequency response is rather stable and flat over a very broad range of frequencies from dc to THz but followed by a series of ionic and electronic resonances at the tail ends of this frequency spectrum [12,13]. Rupprecht and Bell have reported the X band (8.2–12.4 GHz) ε_r of 323 for STO single crystal [14]. Far-infrared spectroscopic ellipsometry of ceramic STO samples at RT have claimed that, due to the hardening of the soft mode, the intrinsic ε_r in the terahertz (THz) region decreased monotonically from ~320–280 with increasing concentration of oxygen vacancies [15].

In displacive ferroelectrics, the transition from the paraelectric to tetragonal ferroelectric state occurs at T_o when the soft mode frequency approaches zero. At T_o, composition and phase-dependent anomalies in ε_r (10^4–10^5) are observed. Below T_o, the non-cen-

trosymmetric material is in the ferroelectric state, in which the overall spontaneous polarization is electrically-switchable at fields greater than the coercive field, E_c. The voltage dependence of the reversible polarization component can be determined by integrating the small-signal, capacitance (or ε_r)–voltage characteristic; note, ε_r is an intrinsic (bulk or volume) property of a single domain crystal. In tetragonal, ferroelectric barium titanate ($BaTiO_3$) single crystal, the prototypical end member of BST, the electronic (e) and phonon-dominated ionic (ph) contributions to the anisotropic ε_r, parallel ($\parallel$) and perpendicular ($\perp$) to the polar c-axis, are as follows: $\varepsilon_{\parallel}^{e} = 5.8$, $\varepsilon_{\parallel}^{ph} = 56$, $\varepsilon_{\perp}^{e} = 5.5$, and $\varepsilon_{\perp}^{ph} =$ 1800–2200. Note, each contribution is constant down to ~1 GHz below which *extrinsic* contributions dominate [16].

For typical displacive-type ferroelectrics with C~10^5 K, ε_r~500 at $T = (T_o + 200\ K)$, but ε_r can be significantly altered up to 100 GHz in the paraelectric and ferroelectric states due to extrinsic effects. In addition to the high ε_r in the ferroelectric state, extrinsic contributions to the ε_r occur from various sources, especially in nanocrystalline, polydomain thin-film materials. Substrate, physical size, and process-induced effects include microstructural evolution, chemical inhomogeneity, non-stoichiometry, micro- and nanopolar entities, localized distortions, and strains due to imperfections, doping, and compensated dipolar defects [17]. Noteworthy are the formation, motion, and/or vibration of electrostatic energy-minimizing, ferroelectric 180° domains, and strain energy-minimizing ferroelastic, non-180° domains [18–20].

The extrinsic contributions to the polarization and ε_r in the paraelectric state above T_o, that can break the centric macroscopic symmetry, also stem from polar entities characterized as precursors to the ferroelectric state [21–23]. For instance, the existence of micro- or nano-polar regions is manifested by spatial variation in magnitude of the polarization, induced piezoelectricity, and non-linear behavior of dielectric properties, electrostrictive strain, and thermal expansion. Some documented reports include defect-induced polar regions [24], nano-polar, residual ferroelectric domains [25], micropolar regions [26], pyroelectricity [27], and flexoelectricity [28]. Additionally, specific illustrations of extrinsic contributions in ceramic and thin-film ε_r are as follows. In the temperature range of 270–1000 K, the X band (8.2–12.4 GHz) ε_r for polycrystalline BST-0.5 ceramic, with T_o of 227 K and C of 7.8×10^4 K, is reported to be 1117 [14]. Subramanyam et al. have reported ε_r as high as 1200 at 10 GHz for nanostructured BST-0.6 thin films on sapphire substrate [29]. The ε_r and dielectric tunability increased with the increase in the film thickness. For a direct comparison, the observed ε_r of nanocrystalline epi-BST-0.5 thin films of the current study were: $\varepsilon_{MgO}^{BST-0.5} = 1420 > \varepsilon_{STO}^{BST-0.5} = 1390 > \varepsilon_{LAO}^{BST-0.5} = 1150$ at 8.2 GHz but are highly frequency dependent (discussed later).

2.2. Engineering of Permittivity by Homogenous Strain in Perovksite Oxide Thin Films

In thin films, the out-of-plane direction is stress-free, whereas the in-plane biaxial stress is primarily due to the (a) difference in thermal expansion between film and substrate during synthesis at elevated temperatures; (b) lattice mismatch between crystalline lattices of the thin film and substrate during heteroepitaxial growth. Thus, biaxial strain manipulation, also known as strain engineering, are currently used to engineer material properties such as electronic band structure, charge transport, dielectric, magnetic, and optical phenomena [30]. Strain engineering, which has been utilized in semiconductor manufacturing technology and has enabled the deposition of strained, single crystal, epitaxial films, has been extended to perovskite oxide thin films and heterostructures for the manipulation of ferromagnetic, dielectric, ferroelectric, piezoelectric, and thermoelectric behavior [31–34]. By considering the effect of internal stresses within the Landau–Ginzburg–Devonshire (LGD) phenomenological formalism for epitaxial single crystals and single domain ferroelectric films, where frequency is not a parameter, various investigators have predicted the appearance of unusual phases and phase transformations. Since strain and electrical polarization are coupled, modifying the in-plane strain state should

result in a change in polarization and the dielectric response. Pertsev and coworkers calculated the misfit (homogeneous) strain–temperature phase diagrams for epitaxial STO, $BaTiO_3$ (BTO), and $PbTiO_3$ (PTO) films and predicted effects of stresses on the phase transformation behavior, existence of unusual ferroelectric phases that are not possible in single crystals and bulk ceramics, and unusual dielectric responses with strain [35–40]. Moreover, Ban and Alpay [40] established theoretical misfit strain–temperature phase diagrams for single domain, epitaxial BST films on cubic substrates. They also provided theoretical estimation of the ε_r of (001) $Ba_{0.7}Sr_{0.3}TiO_3$ (BST-0.7) and BST-0.6 films on (001) Si, MgO, LAO, and STO substrates as a function of misfit strain and film thickness but also with no discussions on frequency dependences. While a monotonic increase in the ε_r with increasing film thickness was estimated for films on LAO and STO substrates, a substantial increase in the ε_r of films due to a structural instability at ~40 nm was predicted for films on MgO substrates. Such theoretical approaches that predict the unusual trends of ε_r may provide guidance for practical, experimental research on materials for microwave devices, but their eventual validity can only be ascertained by comparison with experimental data over a broad frequency range on both single domain (single crystal) and polydomain (and nanocrystalline) films. Ironically, despite the vast literature reports on strain engineering of perovskites, no data or discussion on ε_r, measured over a broad microwave frequency range, of epitaxial single crystalline films by any vapor deposition techniques, have been reported to date, and neither have intrinsic and extrinsic contributions to the ε_r been quantitatively determined.

The extrinsic enhancement of ε_r may also be attained by strain via the creation of polydomain structures in nanocrystalline and epitaxial ferroelectric films, whose dielectric properties may not be bounded by the intrinsic limits of a defect-free and single domain bulk [41,42]. A recent study by Gu et al. [42] reported resonant domain-wall enhanced dielectric tunability and quality factor (Q) in BST thin films on $SmScO_3$ substrate. The nanostructured BST-0.8 thin film with moderate in-plane tensile strain, exhibited resonant nanoscale domain walls and very high Q (>10^5) up to 10 GHz that was comparable to bulk single crystals. Thus, a large dielectric tunability and low dielectric loss tangent were simultaneously achieved in these films. Moreover, various reports on strain-engineered BST thin films have been documented in the literature but no clear distinctions between intrinsic and extrinsic contributions to the measured dielectric properties have been made [43–52]. The approaches have included fabrication on different substrates [43], different film thicknesses [44], different orientation of crystalline substrates [44–47], different buffer layers on Si substrates [48,49], and platinized Si substrates [50]. Campbell et al. fabricated a series of nanostructured ferroelectric thin films of BST-0.6 on LAO substrates using a pulsed laser deposition system with real-time, in situ process control [51]. The dielectric constant increased with increasing compressive misfit strain in very good qualitative agreement with predictions after Ban and Alpay [40] for the ferroelectric cubic (c) phase. In general, ε_r of epitaxial BST thin films shows dispersive behavior at microwave frequencies, stabilizing above 30 GHz [46]. Most of the previous studies only analyzed over a limited bandwidth [42–50], at a single frequency [47] or multiple discrete frequencies [50]. Hence, successful implementation of BST films as electrically tunable dielectrics in microwave devices requires an understanding of both their processing and frequency-dependent dielectric properties [51,52] but with careful considerations of conflating issues of strain and intrinsic/extrinsic effects [17].

3. Experimental Section

The deposition parameters for cubic (paraelectric) BST-0.5 thin-film composition by pulsed laser deposition (PLD) in this study were guided by a previous study on the deposition of epitaxial and nanocrystalline ferroelectric BST-0.6 thin films on (100) LAO single crystal substrates by PLD [51]. In that previous study, the effect of PLD deposition parameters (i.e., growth temperature, energy density of chamber oxygen partial pressure, target-substrate distance, laser pulses, target scan pattern, and pulse repetition rate) on the grain

size, roughness, oxygen deficiency, and microwave properties were thoroughly evaluated [51]. The oxygen partial pressure (pO_2) of 75 mT during the PLD process yielded an average grain size <100 nm for the BST-0.6 thin films on LAO substrates. In the current study, ceramic powders and targets were synthesized in house using the solid-state reaction route; note, details of the procedures are reported elsewhere [52]. The BST-0.5 thin films (600 nm) were deposited on isotropic substrates (i.e., (100) STO, (100) MgO, and (100) LAO single crystals) by PLD using an LPX-210 LambdaPhysik GmbH KrF excimer laser, operating at 248 nm with a pulse energy of 250 mJ and pulse repetition rate of 10 Hz. For a growth rate of ~4 nm/min for BST-0.5 thin films, the substrate temperature was maintained at 720 °C during deposition, and oxygen partial pressure (pO_2) in the chamber was fixed at 80 mTorr to minimize oxygen deficiency and decrease surface roughness in stoichiometric BST-0.5 thin films. Note, reflection high-energy electron diffraction (RHEED) is a high-sensitivity surface science tool for determining the crystalline quality of substrate and thin films [53]. Therefore, the epitaxial growth modes and textured growth of BST-0.5, phase formation, and orientation of the thin films were routinely monitored in situ by RHEED and in real time, and ex situ, by X-ray diffraction (XRD). The RHEED (Staib Instruments RH30) patterns were recorded at 24 keV beam energy and 1.4 A filament current, and XRD in Bragg–Brentano geometry was carried out Rigaku D/Max Ultima III X-ray diffractometer using Cu-Kα_1 radiation.

The dielectric properties of the as-deposited and unannealed BST thin films were determined at microwave frequencies (1–40 GHz) using coplanar waveguide (CPW) transmission line test structures, using conformal mapping techniques, described elsewhere [54]. The CPW test structures were designed for a simple shadow-mask electrode deposition process on the BST thin films. The dimensions of the gaps and widths were chosen based on the limits of a laser-machining process for the fabrication of the shadow masks used. The center conductor width was chosen as 200 μm, with the gaps between the center conductor and the ground lines chosen as 100 μm. The ground lines were 750 μm wide. The test structures were probed using standard ground-signal-ground (GSG) probes with a 250 μm pitch and transmission lines of 5 mm length. A 0.85 μm thick Ti/Pt/Au thick electrode stack was deposited through a shadow mask by electron beam deposition to form the CPW transmission lines on BST thin films. Based on the conductor thickness, the frequency at which the conductor thickness was higher than the skin depth was approximately 8 GHz. Although the total measured insertion loss was accurate, it was difficult to separate the dielectric and conductor losses below 8 GHz due to the conductor thickness. While the relative dielectric permittivity was accurate over the broadband frequencies up to 40 GHz, the loss tangent was only accurate above 8 GHz. The technique for the extraction of dielectric properties of thin films using the CPW transmission lines are detailed elsewhere [54]. Please note that CPW test structures were only fabricated on five 1 cm × 1 cm substrates each of LAO, MgO, and STO.

Table 1 lists properties and parameters of the BST-0.5 thin-film composition and isotropic substrates used in this study, along with theoretical estimates of percent strain due to film-substrate thermal expansion and lattice mismatches. The latter scales with ($\alpha_f - \alpha_s$) and ($T_{Dep} - T_{RT}$), where α_f and α_s are the reported coefficients of thermal expansion of substrate and BST-0.5 composition, respectively, T_{Dep} is the thin-film deposition temperature (720 °C), and T_{RT} is room temperature (25 °C). The percent (%) lattice mismatch or nominal in-plane strain at T_{RT} may be estimated using $(a_s - a_f)/a_s$, where, a_s and a_f are reported lattice parameters of the isotropic substrates and free standing (or unconstrained) cubic BST-0.5 film, respectively, at T_{RT} [40].

Table 1. Properties and parameters of isotropic substrates and a freestanding (or unconstrained) cubic BST-0.5 film with estimated percent strains due to film-substrate lattice mismatch at T_{RT} = 25 °C and T_{Dep} = 720 °C, and film-substrate thermal expansion mismatch.

Substrates & BST Film	Crystal Structure/ Space Group	Thermal Expansion Coefficient, α (10^{-6} K^{-1})	% Thermal Mismatch	Lattice Parameter, a (nm)	% Lattice Mismatch
				T_{RT}	T_{RT}
MgO	Cubic/$Fm\bar{3}m$	12.8	−0.195	0.4216	6.4
$SrTiO_3$ or STO	Cubic/$Pm\bar{3}m$	10.9	−0.063	0.3905	−1.1
$LaAlO_3$ or LAO	Cubic/$Pm\bar{3}m$	9.2	0.056	0.3789	−4.2
$Ba_{0.5}Sr_{0.5}TiO_3$ or BST-0.5 thin film	Cubic/$Pm\bar{3}m$	10	—	0.3947	—

4. Results and Discussions

4.1. Deposition and Characterization of BST-0.5 Films by PLD

At deposition temperature (T_{Dep}), the lattice mismatch between the BST-0.5 film and STO substrate was −0.99%, and a tensile stress existed at the interface during the early stages of deposition. A time sequence of RHEED patterns, observed during the growth of a (100) BST-0.5 thin film on commercial single crystal (100) STO substrate at 720 °C, is illustrated in Figure 1. Prior to growth, the flat substrate had a strong specular reflection and very little streaking, which indicates a smooth diffracting surface with long-range coherence or large terrace size [55]. Also, the absence of characteristic surface reconstructions patterns is indicative of film stoichiometry. Following the sharp RHEED pattern of the STO substrate (t = 0 s), and upon increasing thickness with time, the RHEED patterns began to exhibit well-contrasted streaky lines (t = 20 s and 100 s) as expected for a 2D, layer-by-layer growth mode. With time, the sharp streak pattern turned into spots (t = 250 s and 1000 s), which characterizes a rougher surface with 3D, island growth mode [56–59]. The sharp RHEED features, along with well defined streaks and spots, indicate a flat surface and good nanocrystalline quality of epitaxial BST-0.5 film, with Stranski–Krastanov growth mode.

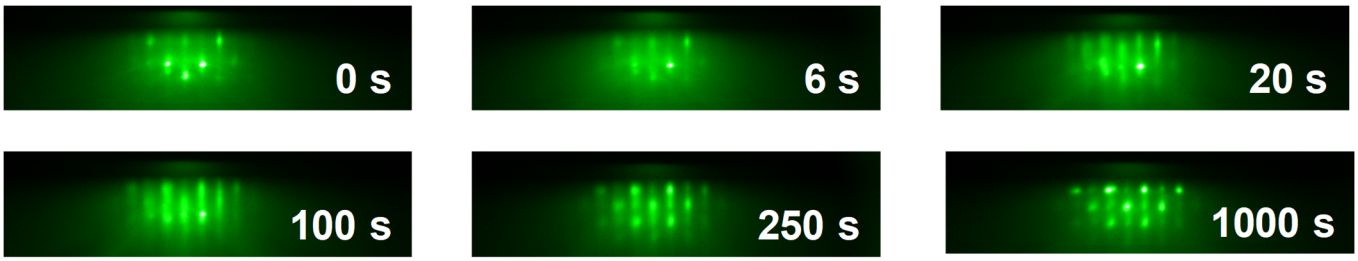

Figure 1. Representative RHEED patterns along [100] azimuth observed during the growth of (100) BST-0.5 thin film on single crystal (100) STO as a function of time, and therefore, increasing film thickness. Note, very little streaking in (100) STO substrate prior to deposition (t = 0 s) is indicative of a diffracting surface with long terraces.

In contrast, the lattice mismatch between the BST-0.5 film and MgO substrate at T_{Dep} was +6.58%, and a compressive stress existed at the interface during the early stages of deposition. A time sequence of RHEED patterns, observed during the growth of a (100) BST-0.5 thin film on commercial single crystal (100) MgO substrate at 720 °C, are illustrated in Figure 2. The MgO substrate had a strong specular reflection and very little streaking, which indicates a smooth diffracting surface with long-range coherence. In addition, Kikuchi lines observed (t = 0 s) in the RHEED image indicate the cleanliness and long-range order of the substrate. Following an initial decline in intensity of the sharp RHEED pattern within a few seconds along the [100] azimuth, and upon increasing thickness with time, the pattern turned directly into spots (t = 25 s and 50 s), which characterizes a rougher surface with direct 3D, island (or Volmer–Weber) growth mode of epitaxial

BST-0.5 thin film on MgO. A single RHEED pattern along the [110] azimuth at 10^4 s is illustrated in the extreme RHS panel in Figure 2, again indicating the nanocrystalline quality of epitaxial BST-0.5 film on MgO.

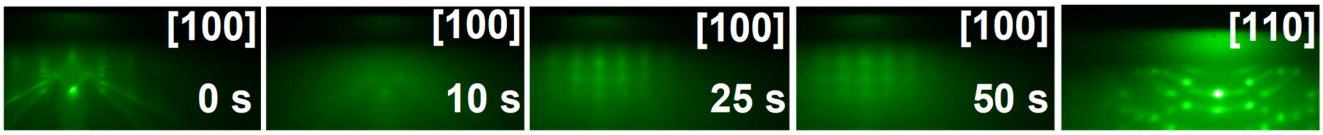

Figure 2. Representative RHEED patterns observed during very early stage of the growth of (100) BST-0.5 thin film on single crystal (100) MgO $SrTiO_3$ as a function of time in seconds, and therefore, increasing film thickness. Note, the very sharp substrate pattern (at t = 0 s) quickly turns into spots (t = 25 s and 50 s) along the [100] azimuth. A pattern along the [110] azimuth at 10,000 s is in the extreme right panel.

The phase purity and crystallinity of the deposited BST-0.5 films were confirmed by X-ray diffraction (XRD) at RT; note, λ = 0.154 nm for Cu-Kα_1. Figure 3 shows a typical θ-2θ scan pattern of an epitaxial BST-0.5 film on single crystal MgO substrate. The sharp characteristic peak at 2θ = 22.36° corresponds to an out-of-plane lattice parameter or spacing (i.e., d_{001} or $a_\perp$) of 0.3973 nm. Similar diffraction patterns but with different values for 2θ peak, and, therefore, different lattice parameters and out-of-plane {100} orientations, were observed in films on STO (2θ = 22.25°; d_{001} = 0.401 nm) and LAO (2θ = 22.56°; d_{100} = 0.394 nm). For all films on single crystal substrates, only the {100} family of peaks appeared, which implies that these single-phase films have in-plane, strain-dependent, cube-on-cube epitaxial relationships with the substrates.

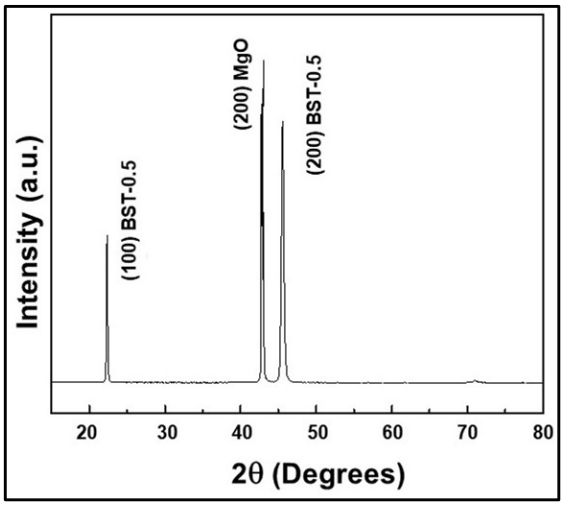

Figure 3. X-ray diffraction (XRD) pattern of BST-0.5 film, under in-plane compression, on single crystal (100) MgO substrate. The peak at 2θ = 22.36°, the out-of-plane lattice spacing (i.e., d_{001} or $a_\perp$) was calculated to be 0.3973 nm, which is higher than the interplanar spacing, d_{001} (0.3947 nm), of unconstrained or freestanding cubic BST-0.5 film.

4.2. Substrate-Dependent in-Plane Strain in BST-0.5 Films

The residual in-plane strain, compressive or tensile, in a perovskite thin film on various substrates (single crystal, polycrystalline, and glassy) is dependent on several factors, including (a) film-substrate coefficient of thermal expansion mismatch; (b) film-substrate lattice mismatch; (c) phase transformation and modification of the crystal symmetry with attendant cation–anion displacements (e.g., ferroelectric–paraelectric); (d) tilt, distortion, and rotation of TiO_6 octahedra (e.g., antiferrodistortive octahedral rotations); (e) chemical strain (e.g., for example, defect-induced lattice parameter change due to change in the chemical environment such as formation of oxygen vacancies); (f) epitaxial (i.e., cube-on-cube) versus nanocrystalline (e.g., textured, randomly oriented) films; (g) presence of

buffer layers; (h) pitch/thickness of individual layers in a multilayer superlattice; (i) strain relieving dislocation formation; (j) film growth temperature; (k) film thickness [30–37,50,60–62].

The strain due to oxygen vacancies are perhaps lower (but highly substrate dependent) due to PLD deposition at a high pO_2 of 80 mTorr, and the absence of paraelectric–ferroelectric transition eliminates strains due to phase transformation [50,63]. For the evolution of in-plane strains during PLD deposition of (100) BST-0.5 thin films of cubic paraelectric composition, undergoing cube-on-cube epitaxial growth on (100) single crystal substrates, thermal expansion mismatch and lattice mismatch are important factors for consideration. At the early stage of deposition at 720 °C, due to the lattice mismatch between BST-0.5 thin-film lattice and substrate during heteroepitaxial growth, the film is homogeneously strained into registry with the substrate in the interfacial plane and is in the so called "pseudo-morphic state". Upon increasing thickness, the build-up of elastic strain energy makes the epitaxial film unstable, and at a critical thickness (h_c), the strain energy is relieved and eventually reduces to zero by the introduction of misfit dislocations at the interface. Consequently, a relaxed film is formed with its natural deposition-temperature lattice parameter. Typically, h_c for perovskite oxide films can range from 1 monolayer (~0.4 nm) to hundreds of monolayers [64–67]. Since the BST-0.5 films here were 600 nm thick and significantly above h_c, they were relaxed at the growth temperature (T_{dep}). Earlier, RHEED revealed Stranski–Krastanov (i.e., layer-plus-island) and Volmer–Weber (i.e., three-dimensional island) growth modes of BST-0.5 film on STO and MgO substrates, respectively. Such mechanisms facilitate the nucleation of dislocations in oxide films, which assist the strain relaxation at T_{dep} [68,69]. Note, edge dislocations, uniformly distributed along the entire BST-0.5/LAO interface, and both edge and threading dislocations in BST-0.5/MgO to relieve misfit stresses have been previously observed by high-resolution transmission electron microscopy [70,71]. To estimate the in-plane strains in epitaxial BST-0.5 on single crystal substrates, two assumptions are made, namely, (a) the coefficient of thermal expansions of film and substrate are constant, and (b) additional formation of dislocations during cooling from 720 °C to RT is minimal. Thus, any in-plane biaxial strain ($\epsilon_{\parallel}$) upon cooling to RT is predominantly due to thermal strain (column 4 in Table 1) and may be calculated using

$$\epsilon_{\parallel} = \frac{a_{\parallel} - a_{RT}}{a_{RT}} \quad (1)$$

where, $a_{//}$ is the in-plane lattice parameter of a constrained BST-0.5 film at RT (and estimated below using STO-BST as an example of a film-substrate pair), and a_{RT} = 0.3947 nm is the lattice parameter of an unconstrained BST-0.5 film at RT (Table 1). As the BST-0.5 film cools down to RT and becomes strained into compression by the rigid and thick STO substrate due to thermal expansion mismatch, the net change in the in-plane lattice parameter of BST-0.5 will not only be dictated by the magnitude of the net change in the in-plane lattice parameters of STO but also must match it. Therefore,

$$a_{T_{dep}}^{STO} - a_{RT}^{STO} = a_{T_{dep}}^{\mathrm{BST-0.5}} - a_{RT}^{\mathrm{BST-0.5}} \quad (2)$$

$$or, \qquad a_{\parallel} = a_{RT}^{\mathrm{BST-0.5}} = a_{720\,^{0}C}^{\mathrm{BST-0.5}} - \left(a_{720\,^{0}C}^{STO} - a_{25\,^{0}C}^{STO}\right) \quad (3)$$

Using the RT literature data and the estimated T_{dep} data given in Table 1 (and reiterated in Table 2), the in-plane lattice parameter of BST-0.5 thin film on STO is estimated as

$$\boldsymbol{a_{\parallel} = 0.3974 - (0.3935 - 0.3905) = 0.3944\ nm} \quad (4)$$

Therefore, the percent in-plane strain (Equation (1)) in BST-0.5 thin film on STO is found to be

$$\boldsymbol{\epsilon_{\parallel} = \left(\frac{a_{\parallel} - a_{RT}}{a_{RT}}\right) \times 100 = \left(\frac{0.3944 - 0.3947}{0.3947}\right) \times 100 = -0.076\%} \quad (5)$$

Similarly, the calculated (biaxial) percent in-plane strain in BST-0.5 thin film on MgO is also negative (i.e., compressive), but on LAO, the in-plane (biaxial) strain is tensile (Table 2).

Table 2. *In-plane* lattice parameters ($a_{||}$) and percent (%) *in-plane* strain (biaxial compressive or tensile) at RT in constrained BST-0.5 films deposited on single crystal substrates. The cubic lattice spacing of unconstrained BST-0.5 thin film at RT (a_{RT}) and 720 °C ($a_{720\,°C}$), as well as for substrates at these temperatures are taken from Table 1.

Substrates and BST Film	Lattice Parameter, a (nm)		In-Plane Lattice Spacing ($a_{||}$) of Constrained BST-0.5 Film (nm)	% In-Plane Strain ($\epsilon_{||}$) in BST-0.5 Film	State of in-Plane Strain in BST-0.5 Film
	RT = 25 °C	T_{Dep} = 720 °C			
MgO	0.4216	0.4254	0.3936	−0.279	Highly Compressive
STO	0.3905	0.3935	0.3944	−0.076	Moderately Compressive
LAO	0.3789	0.3813	0.3950	+0.076	Moderately Tensile
Unconstrained or relaxed BST-0.5 film	0.3947	0.3974	—	—	—

4.3. Relative Locations of Nanocrystalline epi-BST-0.5 Films within Primary Phase Fields of Calculated "Temperature-in-Plane Strain" Diagram with Predicted Dielectric Anomaly

Based on the LGD phenomenological models [36–40,50,72] and results of density functional theory [73], theoretically calculated temperature (T)-in-plane strain ($\epsilon_{||}$) phase diagrams for {100}- and {111}-oriented, single domain and epitaxial $Ba_xSr_{1-x}TiO_3$ films (i.e., BST-x with x = 1.0, 0.9, 0.8, 0.7, 0.6, 0.4, and 0.2) have been well documented in the literature. Against the backdrop of this knowledge, and to reconcile and/or contravene experimental microwave results of this study, a schematic T-$\epsilon_{||}$ phase diagram for nanocrystalline (100) epi-BST-0.5 film is shown in Figure 4 (not-to-scale). The theoretically calculated phase diagram predicts three, homogenous strain-dependent primary phase fields: paraelectric (***P***) within moderately compressive and tensile zones centered around zero strain, with the width spanning roughly 1%.

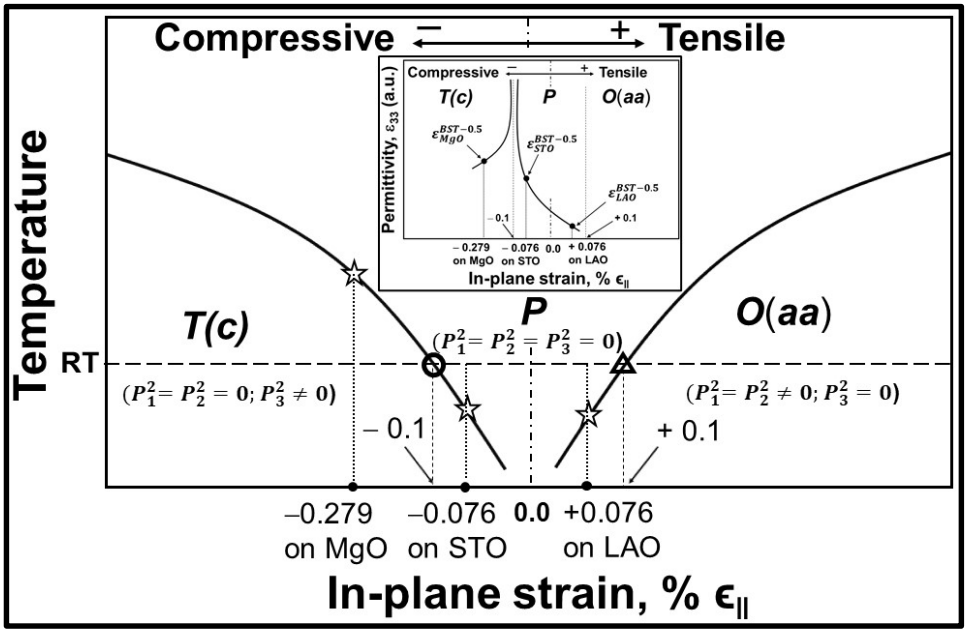

Figure 4. Schematic temperature (T) in-plane strain ($\epsilon_{||}$) phase diagram (not-to-scale) for single domain and epitaxial (100) BST-0.5 film under in-plane compressive and tensile strains on cubic substrates. The theoretically calculated Curie–Weiss (CW) temperatures, represented by open circle (O) at % compressive $\epsilon_{||}$ of −0.1 and open triangle (Δ) at % tensile $\epsilon_{||}$ of +0.1, correspond to ***T(c)-P*** phase boundary and ***P–O(aa)*** phase boundary, respectively, at RT. The open stars (☆) correspond to the relative CW temperatures of nanocrystalline epi-BST-0.5 films. The inset (not-to-

scale) shows the theoretically predicted anomaly in $\epsilon_{\|}$-dependent, out-of-plane dielectric permittivity (ε_{33} *or* $\varepsilon_{\perp}^{/}$) of single domain film at RT in the vicinity of the ***T(c)-P*** phase boundary; note, the tails of $\varepsilon_{\perp}$ and the relative position coordinates ($\epsilon_{\|}$, $\varepsilon_{\perp}^{/}$) of nanocrystalline epi-BST-0.5 films, denoted as solid circles (•), are a guide to the eye.

$\boldsymbol{\epsilon_{\|}}$ of ±0.1 at RT, and two low-symmetry phase fields: tetragonal (***T***(***c***)) in the high compression zone and orthorhombic (***O***(***aa***)) in the high tensile zone [74]. The nanocrystalline epi-(100) BST-0.5 on STO and MgO should lie in the ***P*** phase field and ***T(c)*** phase field, respectively, near the ***P-T(c)*** phase boundary in the compression zones. Based on data in Table 2, a film with high in-plane compression strain (tetragonality >> 1) on MgO at RT and within the ***T(c)*** phase will be on the left side of the ***T(c)-P*** phase boundary. In essence, the in-plane compressive strain (i.e., epilayer compressed in the lateral direction) will be accommodated by out-of-plane tetragonal distortion. Note from Figure 3, the out-of-plane lattice spacing (i.e., d_{001} or $a_{\perp}$) of constrained BST-0.5 film on MgO was found to be 0.3973 nm, which is higher than the interplanar spacing, d_{001} (0.3947 nm), of unconstrained or freestanding cubic BST-0.5 film. However, a pseudo-cubic film on STO, with moderate in-plane compression strain (tetragonality ≥ 1), is predicted to be on the right side of the ***P-T(c)*** phase boundary and within the ***P*** phase. Conversely, a pseudo-cubic and epitaxial (100) BST-0.5 films on LAO with moderate in-plane tensile strain (tetragonality ≤ 1) is predicted to be on the left side of the ***P-O***(***aa***) phase boundary and within the ***P*** phase.

It is also relevant to note that according to theoretical predictions [34–40,50,72–76], the Curie–Weiss constants and Curie–Weiss temperatures change with misfit strain. In addition, strain-based transformations due to structural instabilities via polarization expansion/contraction or rotation at the ***T(c)-P***, ***P-O***(***aa***), and ***P-M***(***r***) boundaries lead to strain-mediated (i) rapid variation in the components of the polarization and, consequently, (ii) unusually large or anomalous dielectric (shown in the inset of Figure 5) and piezoelectric responses. The out-of-plane relative dielectric permittivity ($\varepsilon_{\perp}^{/}$) exhibits a Curie–Weiss-type anomaly in both the temperature and in-plane strain ($\epsilon_{\|}$) dependences and, contingent on external conditions, the anomaly can exhibit features corresponding to the second or first order ferroelectric phase transitions. In the qualitative representation of T-$\epsilon_{\|}$-structure behavior in Figure 4, the open stars (☆) are the relative Curie–Weiss temperatures of nanocrystalline epi-BST-0.5 films within the phase diagram. The renormalized out-of-plane Curie–Weiss constant ($C_{\perp}$) and out-of-plane Curie–Weiss temperature ($T_{\perp}$) of BST-0.5 film, constrained via moderate in-plane compression strain on isostructural STO, was estimated using the following relations and with data reported in the literature [36,74]

$$C_{\perp}^{-1} = C^{-1} - 2\varepsilon_0\left[2\left(\frac{Q_{12}}{s_{11}+s_{12}}\right) - \frac{2\nu}{1-\nu}\left(\frac{Q_{11}}{s_{11}+s_{12}}\right)\right](\alpha_s - \alpha_f) \quad (6)$$

$$or, \qquad C_{\perp}^{-1} = C^{-1} - 2\varepsilon_0\left[2q_{12} - \frac{2\nu}{1-\nu}q_{11}\right](\alpha_s - \alpha_f) \quad (7)$$

$$T_{\perp} = \frac{C_{\perp}}{C}\left[T_0 + 2C\varepsilon_0\left(2q_{12} - \frac{2\nu}{1-\nu}q_{11}\right) \times [\epsilon_{\|}]\right] \quad (8)$$

where, C (1.135×10^5 K) is the Curie–Weiss constant of unconstrained BST-0.5 film, ε_0 (8.854×10^{-12} Fm^{-1}) is the permittivity of free space, Q_{12} (−0.034 m^{4}C^{-2}) is the electrostrictive coefficient, s_{11} (4.33×10^{-12} m^{2}N^{-1}) and s_{12} (-1.39×10^{-12} m^{2}N^{-1}) are the elastic compliances, T_o (237.7 K) is the Curie temperature of an unconstrained BST-0.5 film, ν (0.23) is the Poisson's ratio, $\epsilon_{\|}$ (-7.6×10^{-4}) is the in-plane strain (Table 2), and α_f and α_s are the thermal expansion coefficients of the film and substrates (Table 1), respectively. The calculated values of $C_{\perp}$ and $T_{\perp}$ were found to be 1.064×10^5 K and 285 K, respectively. In essence, in film (f)-substrate (s) couples where $\alpha_f < \alpha_s$ (i.e., BST-0.5 films under in-plane compression on MgO and STO), $C_{\perp}<C$ and $T_{\perp}>T_o$, and vice versa for BST-0.5 film under

in-plane tension on LAO; results that are consistent with previous reports [36,74]. Additionally, the inset in Figure 5 (not-to-scale) shows the predicted anomaly in $\epsilon_{||}$-dependent, $\varepsilon_{\perp}^{/}$ at RT in the vicinity of the ***T(c)-P*** phase boundary but, note again, with absolutely no mention of any frequency (f) dependence of permittivity, $\varepsilon_{\perp}^{/}(f)$. With a dielectric permittivity, $(\varepsilon^{/})^{-1}$, of 1500 for unconstrained BST-0.5 film, the $\varepsilon_{\perp}^{/}$ of BST-0.5 film, constrained via moderate in-plane compression strain on isostructural STO, is estimated to be 12,206 by using the following relation

$$\left(\varepsilon_{\perp}^{/}\right)^{-1} = \left(\varepsilon^{/}\right)^{-1} - 2\varepsilon_0\left(2q_{12} - \frac{2\nu}{1-\nu}q_{11}\right) \times [\epsilon_{||}] = \left(\varepsilon^{/}\right)^{-1} - \left[\frac{T_{\perp}}{C_{\perp}} - \frac{T_0}{C}\right] \quad (9)$$

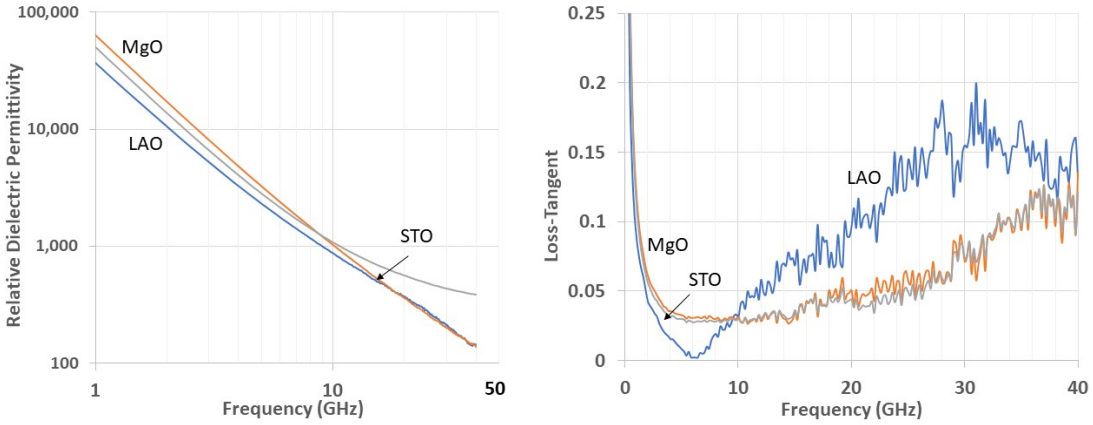

Figure 5. Frequency-dependent, out-of-plane, dielectric properties of BST-0.5 films on crystalline substrates at RT and zero bias.

The theoretically predicted tails of $\varepsilon_{\perp}^{/}$ in BST-0.5 and the relative location or position coordinates ($\epsilon_{||}$, $\varepsilon_{\perp}^{/}$) of BST-0.5 films are only qualitatively represented. Note, one tail within the ferroelectric ***T(c)*** phase field contains the BST-0.5 film under high in-plane compression on MgO, and the other tail within the paraelectric ***P*** phase field contains both the BST-0.5 film under moderate compression on STO and the BST-0.5 film under moderate tension on LAO. Despite the non-single domain nature of the nanocrystalline epi-BST-0.5 films, the trend in $\varepsilon_{\perp}^{/}$ with in-plane strain is predicted to be as follows: ${}^{BST-0.5}_{MgO}\varepsilon_{\perp}^{/} > {}^{BST-0.5}_{STO}\varepsilon_{\perp}^{/} > {}^{BST-0.5}_{LAO}\varepsilon_{\perp}^{/}$.

4.4. Microwave (1–40 GHz) Properties of BST-0.5 Thin Films at RT and Zero Dc Bias

Figure 5 illustrates the $\varepsilon_{\perp}^{/}$ and dielectric loss tangent, tanδ, of BST-0.5 films on single crystal substrates at RT in the 1–40 GHz range; note, the strong dielectric (relaxation) dispersions with their attendant peaks in tanδ observed below 10 GHz. The experimental data at low frequencies show that the predicted substrate-dependent $\varepsilon_{\perp}^{/}$ holds (i.e., ${}^{BST-0.5}_{MgO}\varepsilon_{\perp}^{/} > {}^{BST-0.5}_{STO}\varepsilon_{\perp}^{/} > {}^{BST-0.5}_{LAO}\varepsilon_{\perp}^{/}$), but here the $\varepsilon_{\perp}^{/}$s are highly frequency dependent, dropping sharply from tens of thousands to ~1000 by 10 GHz.

The overall behavior of epitaxial (100) films on single crystal MgO, STO, and LAO substrates are similar, e.g., $\varepsilon_{\perp}^{/}$ ranges between 1470 (on MgO at 8 GHz) and 146 (on LAO at 40 GHz), with corresponding tan δs of 0.0298 and 0.131, respectively. Up to a frequency of 8.6 GHz, ${}^{BST-0.5}_{MgO}\varepsilon_{\perp}^{/} > {}^{BST-0.5}_{STO}\varepsilon_{\perp}^{/} > {}^{BST-0.5}_{LAO}\varepsilon_{\perp}^{/}$, all epitaxial films exhibit a precipitous drop in $\varepsilon_{\perp}^{/}$ obeying a power law, $\varepsilon_{\perp}^{/} \propto f^{-n}$, with exponent, n, being substrate and frequency range-dependent; the values of n up to 10 GHz, between 10 and 20 GHz, and between 20 and 40 GHz on MgO, STO, and LAO substrates are obtained as follows: n = 1.73, 1736, and 1.75 up to 10 GHz, n = 1.475, 1.49, 1.55 between 10 and 20 GHz, and n = 1.22, 1.25, 1.35

between 20 and 40 GHz, for MgO, STO and LAO substrates, respectively. Overall, the reduction of $\varepsilon_{\perp}^{/}$ with frequency of the film on MgO is the highest, on STO the lowest, and on LAO in between. The tanδ of the epitaxial films increases with frequency above 10 GHz for all the samples. The film on LAO exhibits the highest tanδ and a distinct peak at 32 GHz, the film on STO has the lowest tanδ with MgO in between, but with their loss peaks shifted to higher frequencies at 37 GHz and >40 GHz, respectively.

From the data in Figures 5 and 6, it is clear that the $\epsilon_{\parallel}$–mediated, $\varepsilon_{\perp}^{/}$ of BST-0.5 films are consistent with the theoretically predicted trend of ${}^{BST-0.5}_{MgO}\varepsilon_{\perp}^{/} > {}^{BST-0.5}_{STO}\varepsilon_{\perp}^{/} > {}^{BST-0.5}_{LAO}\varepsilon_{\perp}^{/}$, but all $\varepsilon_{\perp}^{/}$ are not only frequency dependent (N.B., the diminution in $\varepsilon_{\perp}^{/}$ from 10 s of thousands to below 1500 by 10 GHz), that trend breaks down above 8.6 GHz as illustrated in Figure 6. A $\varepsilon_{\perp}^{/}$ of 1308.5 at 8.6 GHz is the crossover point of $\varepsilon_{\perp}^{/}$ between BST-0.5 films on MgO and STO, and $\varepsilon_{\perp}^{/}$ of 416.4 at 18 GHz correspond to the crossover point of $\varepsilon_{\perp}^{/}$ between BST-0.5 films on MgO and LAO. Therefore, a crossover point at 8.6 GHz changes the trend in $\varepsilon_{\perp}^{/}$ to: ${}^{BST-0.5}_{STO}\varepsilon_{\perp}^{/} > {}^{BST-0.5}_{MgO}\varepsilon_{\perp}^{/} > {}^{BST-0.5}_{LAO}\varepsilon_{\perp}^{/}$, and another crossover point at 18 GHz again changes the trend in $\varepsilon_{\perp}^{/}$ to: ${}^{BST-0.5}_{STO}\varepsilon_{\perp}^{/} > {}^{BST-0.5}_{LAO}\varepsilon_{\perp}^{/} > {}^{BST-0.5}_{MgO}\varepsilon_{\perp}^{/}$.

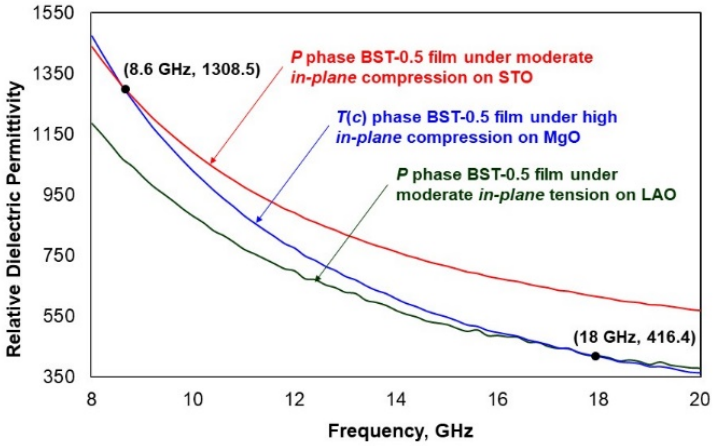

Figure 6. Frequency-dependent, out-of-plane and RT relative dielectric permittivity, $\varepsilon_{\perp}^{/}$, of BST-0.5 films on single crystal substrates at 8–20 GHz with zero dc bias.

4.5. Factors Influencing Microwave Dielectric Responses of BST-0.5 Thin Films

As briefly outlined in the background, contributions to the microwave dielectric response in thin films stem from intrinsic (i.e., electronic, lattice, homogeneous strain,) and extrinsic (e.g., motion of domain and/or phase boundary, short range polar entities) effects. While the former is manifested in both monodomain and polydomain single crystal films, the latter exerts an additional influence on nanocrystalline but epitaxial thin films that are polydomain. Moreover, processing parameters, film thickness, crystalline quality, inhomogeneous strain, and microstructural effects including grain size, defects, and chemical inhomogeneity play important roles. As indicated in past microwave dielectric studies, these extrinsic factors are highly influential below 100 GHz. In this work, the BST-0.5 films on single crystal substrates were deposited under identical conditions: pO_2 80 mTorr and 720 °C. The phase pure, nanocrystalline films, with constant thickness (600 nm) but some grain size variations, clearly exhibit substrate and in-plane strain-dependent microwave dielectric responses. These responses are a result of the juxtaposition, and perhaps coupled effects of homogeneous in-plane strains, nano-polar regions, and strain relieving growth defects (and consequent inhomogeneous strains).

(1) Epitaxial (100) BST-0.5 film, with a high in-plane thermal compression strain ($\epsilon_{\parallel}$) of −0.279% on single crystal MgO substrate, exists on the left of the ***P-T(c)*** phase boundary within the ***T(c)*** phase at RT (Figure 4). Thus, as the polarization component, $P_3^2 \neq$

0 within ***T(c)***, it is ferroelectric. Therefore, due to contributions from (a) intrinsic electronic and homogeneous strain-mediated, lattice (Equation (8)), and (b) *extrinsic* strain energy-minimizing, non-180° ferroelastic, domains and nano-polar regions, the $\varepsilon_{\parallel}^{/}$ is in the tens of thousands at low frequencies. However, reduction in the contributions from homogeneous $\epsilon_{\parallel}$ and such nano-domain regions with frequency, coupled with the presence of spatial strain gradients due to misfit and threading dislocations (Section 4.2) are responsible for the highly dispersive relaxation up to 10 GHz and gradual reduction in $\varepsilon_{\perp}^{/}$ between 10 and 40 GHz [77]. Regardless of the sign of inhomogeneous in-plane strain, the coupling of strain gradient to polarization via flexoelectricity reduces the intrinsic contribution to $\varepsilon_{\perp}^{/}$ [78,79]. Apparently, strain fields surrounding the dislocations also enhance the depolarization fields and higher film thicknesses are required for polarization saturation [17]. Indeed, for a 350 nm PLD BST-0.5 film, it has been demonstrated that a reduction in dislocation density, by ex situ annealing in flowing oxygen at 1150 °C for 24 h, has resulted in an increase in permittivity from 870 (as-deposited) to 2000 (annealed) at 20 GHz [71].

(2) Epi-(100) BST-0.5 film, with a moderate in-plane thermal compression strain ($\epsilon_{\parallel}$) of –0.076% on single crystal STO substrate, exists on the right of the ***P-T(c)*** phase boundary within the ***P*** phase at RT. The polarization component, $P_3^2 = 0$ within ***P***, but since it is pseudo-cubic and within the Curie–Weiss region, strain-based residual ferroelectricity and polar nanoregions makes the material dielectrically active. At very low frequencies, the $\varepsilon_{\perp}^{/}$is in the tens of thousands, but in Section 4.3, the in-plane compression strain-dependent $\varepsilon_{\perp}^{/}$ was estimated to be 12,206. Therefore, rather high, and frequency-dependent extrinsic contributions to the $\varepsilon_{\perp}^{/}$ are unequivocal. Contributions from residual ferroelectricity and/or nano-polar regions, coupled with the intrinsic contribution, makes the overall $\varepsilon_{\perp}^{/}$ lower than that of BST-0.5 film on MgO below 8.6 GHz. However, the crossover (Figure 6) at 8.6 GHz is the direct result of the elimination of frequency-dependent domain contribution in films on MgO and the higher crystalline quality of films on STO due to the Stranski–Krastanov growth mode. The low lattice mismatch of the film at growth temperature (Table 1) minimizes the detrimental effects of dislocations, which are present in low densities. Thus, in the 8–40 GHz range, extrinsic tanδ is lower compared to films on MgO.

(3) Epi-(100) BST-0.5 film, with a moderate in-plane thermal tensile strain ($\epsilon_{\parallel}$) of + 0.076% on single crystal LAO substrate, exists on the left of the ***P-O***(***aa***) phase boundary within the ***P*** phase at RT. The frequency dependence of the dielectric response ($\varepsilon_{\perp}^{/}$ and tanδ) of this film parallels that of STO but is a little inferior because of the expected (a) $C_{\perp}>C$ and $T_{\perp}<T_o$; (b) dislocations (due to high lattice mismatch at growth temperature; Table 1 and Section 4.2); (c) charged oxygen vacancy defects created for strain relief. Note, first-principles calculations have shown that oxygen vacancy defect formation energy is lowered by tensile strain due to an electrostatic effect. This in turn can produce inhomogeneous strain since vacancy concentration gradients represent a special case of strain gradients [80–83].

4.6. Defect Parameter of BST-0.5 Thin Film on STO Using the Vendik and Zubko Model

The phenomenological Vendik and Zubko model considers random built-in electric fields, stemming from the presence of dipolar or charged defects, which suppress dielectric permittivity in paraelectric materials. Additionally, the microwave energy is converted to a low frequency hyper-sound or acoustic phonons that are dissipated by the lattice as dielectric losses [82–86]. This model may be used to determine the defect density and inhomogeneity via the useful defect parameter metric, ξ_s. In essence, ξ_s reflects the statistical dispersion of charged defect-induced biasing field, which is a function of nanocrystalline size, the charge density at their boundaries, and charged imperfections. Moreover, the value of ξ_s correlates with the microwave dielectric loss in the incipient ferroelectrics [85]. The as-deposited, moderately in-plane strained epi-BST-0.5 film on STO

showed a relatively low loss and the highest permittivity up to 40 GHz. Therefore, based on the in-plane strain, film quality, and overall microwave measurement data, the following trend is expected: $\xi_{s_{MgO}}^{BST-0.5} > \xi_{s_{LAO}}^{BST-0.5} > \xi_{s_{STO}}^{BST-0.5}$. The zero bias, out-of-plane relative dielectric permittivity, $\varepsilon_{\perp}^{/}$, of constrained epi-BST-0.5 film on STO, when corrected for in-plane strain via usage of $C_{\perp}$ and $T_{\perp}$, may be represented by the Vendik and Zubko model as follows

$$\varepsilon_{\perp} = \frac{\frac{C_{\perp}}{T_{\perp}}}{\{[\xi_s^2 + \eta(T_{\mathrm{RT}})^3]^{0.5} + \xi_{\mathrm{S}}\}^{\frac{2}{3}} + \{[\xi_s^2 + \eta(T_{\mathrm{RT}})^3]^{0.5} - \xi_{\mathrm{s}}\}^{\frac{2}{3}} - \eta(T_{\mathrm{RT}})}$$

$$\eta(T_{\mathrm{RT}}) = \sqrt{(\theta_D/4T_{\perp})^2 + (T_{\mathrm{RT}}/T_{\perp})^2} - 1$$

where (from Section 4.2), $\varepsilon_{\perp}^{/}$is at T_{RT} = 298 K, $C_{\perp}$ (1.064×10^5 K) is the Curie–Weiss constant of constrained film, $T_{\perp}$ (285 K) is the Curie–Weiss temperature of constrained film, $\eta(T_{\mathrm{RT}})$ is 0.0568, θ_D (175 K) is the Debye temperature of unconstrained BST-0.5 film, and ξ_{s} is the measure of density of defects and inhomogeneity in constrained BST-0.5 film. For the experimentally measured $\varepsilon_{\perp}^{/}$ of 388 at 40 GHz, ξ_{s} is found to be 0.51 for constrained epi-BST-0.5 film on STO; note, high-quality single crystals exhibit a value of ξ_{s} = 0.01–0.2, whereas ξ_{s} = 0.2–1.2 for ceramics and thin films [20,85].

5. Summary and Conclusions

Nanocrystalline and epitaxial, (100)-oriented $Ba_{0.5}Sr_{0.5}TiO_3$ (BST-0.5) thin films (600 nm) were deposited on single crystal MgO, STO, and LAO substrates at an oxygen partial pressure (pO_2) of 80 mTorr and temperature (T) of 720 °C using pulsed laser deposition (PLD). The phase purity and quality of the films were routinely monitored by XRD and RHEED. The broadband out-of-plane microwave (1–40 GHz) dielectric properties of the films were measured using coplanar waveguide transmission line (CPW) test structures.

Using literature data, homogeneous and biaxial in-plane strain ($\epsilon_{\|}$) due to thermal mismatch in the BST-0.5 films on MgO, STO, and LAO substrates were estimated to be:

(a) −0.279% (highly compressive) and predicted to be in the tetragonal/ferroelectric (***T***(***c***) phase,
(b) −0.076% (moderately compressive) and predicted to be in the paraelectric (***P***), and
(c) +0.076% (moderately tensile) and predicted to be in the paraelectric (***P***).

Based on these literature reports on theoretically calculated T-$\epsilon_{\|}$ phase diagrams of and $\epsilon_{\|}$-dependent, out-of-plane dielectric permittivity ($\varepsilon_{\perp}^{/}$) anomalies in single crystal and single domain epitaxial BST-0.5 films, the theoretically predicted $\epsilon_{\|}$-dependent but frequency-independent $\varepsilon_{\perp}^{/}$ in the nanocrystalline films should be in the order: ${}_{MgO}^{BST-0.5}\varepsilon_{\perp}^{/} > {}_{STO}^{BST-0.5}\varepsilon_{\perp}^{/} > {}_{LAO}^{BST-0.5}\varepsilon_{\perp}^{/}$. The experimental data at low frequencies show that the predicted substrate-dependent order of $\varepsilon_{\perp}^{/}$ holds, but the $\varepsilon_{\perp}^{/}$s are highly frequency dependent, dropping sharply from tens of thousands to ~1000 by 10 GHz. Since most of the data measured is in the latter part of the relaxation regime, the inflection point for $\varepsilon_{\perp}^{/}$ is not visible in our measurements. In the low frequency, we see the homogenous strain effects as we observe the relative dielectric permittivity higher than 10,000. The sharp decrease in dielectric permittivity is due to the strong dielectric relaxation effects stemming from multiple mechanisms, which we cautiously surmise at this time. These dielectric relaxations are accompanied by peaks in the loss tangent (tanδ) at frequencies of ≥ 40 GHz, 37 GHz, and 32 GHz for films on MgO, STO, and LAO, respectively.

Guided by numerous data and explanations in the literature, the contributions to the low-frequency $\varepsilon_{\perp}^{/}$ in the films on MgO stems primarily from homogeneous strain, as well as *extrinsic* polydomains, namely, non-180° domains and perhaps nano-polar regions. The relative weights and rate of diminishment of these contributions with frequency give rise to the highly dispersive behavior (i.e., $\varepsilon_{\perp}^{/} \propto f^{-n}$ with n = 1.7, below 10 GHz). Although

these contributions are significantly diminished beyond 10 GHz, the detrimental effects of microstructural defects, where $\varepsilon_{\perp}^{/} \propto f^{-n}$, with n = 1.475 between 10 and 20 GHz and n = 1.22 between 20 and 40 GHz, are manifested with observed crossover points with films on STO and LAO. In the 10–40 GHz range, extrinsic inhomogeneous strain, and spatial strain gradients due to defects and dislocations, stemming from the large lattice mismatch and strain energy relief at the deposition temperature, negatively influences the intrinsic $\varepsilon_{\perp}^{/}$.

In contrast, the contributions to the dispersive low-frequency $\varepsilon_{\perp}^{/}$ in films on LAO stems primarily from reduced homogeneous strain (note, $C_{\perp}>C$ and $T_{\perp}<T_o$), as well as nano-polar regions. Similar, to the films on MgO, these contributions diminish with frequency and the detrimental extrinsic effects of dislocations (due to the high lattice mismatch at growth temperature) and charged oxygen vacancy defects (due to thermally-driven tension) on intrinsic $\varepsilon_{\perp}^{/}$ are manifested at higher frequencies.

The enhanced contributions to the dispersive low-frequency $\varepsilon_{\perp}^{/}$ in isostructural films on STO stems primarily from enhanced homogeneous strain (note, $C_{\perp}<C$ and $T_{\perp}>T_o$), as well as *extrinsic* residual ferroelectricity and/or nano-polar regions. The maintenance of the high $\varepsilon_{\perp}^{/}$ over a wide frequency range (note, 388 at 40 GHz) the higher crystalline quality of films on STO due to the Stranski–Krastanov growth mode, and low dislocation densities in BST-0.5 film due to low lattice mismatch with STO at growth temperature. Using the Vendik and Zubko model, the defect parameter metric, ξ_s, of 0.51 was estimated at 40 GHz. From the observed data, the detrimental effects of extrinsic factors to the intrinsic $\varepsilon_{\perp}^{/}$ at higher frequencies leads to the following trend: ${}^{BST-0.5}_{STO}\varepsilon_{\perp}^{/} > {}^{BST-0.5}_{LAO}\varepsilon_{\perp}^{/} > {}^{BST-0.5}_{MgO}\varepsilon_{\perp}^{/}$.

Here, uncertainties in the interpretation of the microwave dielectric responses have arisen due to the conflation of independent (but weighted) frequency-dependent influences including homogeneous in-plane strain, extrinsic microstructural features such as ferroelastic domains and nano-polar regions, and inhomogeneous strains due to defects. Based on the current data, the extrinsic contributions to the $\varepsilon_{\perp}^{/}$ in the low-frequency end approach 50% of the intrinsic contributions, and both the homogeneous strain-mediated and extrinsic effects are frequency dependent. The influences of inhomogeneous strain on the electronic and lattice components are manifested at the high-frequency end. Undoubtedly, more work is warranted to validate the assumptions in this qualitative and preliminary discussion based on the rich literature reports. However, to leverage strain engineering for practical applications, quantitative and comprehensive in situ, and ex situ physicochemical and electrical characterization of thin films from a single source with known (and controlled) processing history, are necessary to (a) quantify the intrinsic and extrinsic responses and (b) understand and control their reproducibility and reliability. A low growth rate of the nanocrystalline epi-BST epilayers on well-characterized substrates of high quality, coupled with in situ or ex situ oxygen annealing, may be favorable to reduce the influences of extrinsic factors. These issues and concerns further underscore the need and importance of understanding the intricate interrelationships between substrate-dependent BST structure (unit-cell parameters, epitaxial crystalline quality, roughness, grain size, grain orientation, grain boundary density, defects, and domain size and density), processing (substrate type, orientation, and quality, and oxygen partial pressure, temperature, deposition rate, and ex situ annealing), and microwave property (frequency, voltage, and temperature dependence) of both pseudo-morphic and relaxed BST films by PLD. Eventually, control of these structure–processing–microwave property interrelationships will lead to enhanced dielectric properties and tunability of BST over a broadband millimeter-wave frequency, and the realization of applications such as reconfigurable front ends for 5G communications technology.

Author Contributions: Investigation, S.K.D., S.K., S.P.P., R.S.K. and G.S. All authors contributed to the manuscript. All authors have read and agreed to the published version of the manuscript.

Funding: This research was partly funded by DoD-AFOSR Grant #FA9550-20-1-0064.

Institutional Review Board Statement: Not Applicable.

Informed Consent Statement: Not Applicable.

Data Availability Statement: Authors are willing to share measurement results from this publication upon request via email.

Acknowledgments: This work was partially supported by the DoD-AFOSR Grant #FA9550-20-1-0064. SKD acknowledges discussions of the Curie–Weiss behavior and the Vendik & Zubko model with his student Shiva Mittal, and consultation with his colleague S. Trolier-McKinstry at Penn State on strain and extrinsic effects. GS thanks his former PhD students Hailing Yue and Shu Wang for their help with the experimental measurements of the samples.

Conflicts of Interest: Authors declare no conflict of interest.

References

1. Subramanyam, G.; Cole, M.W.; Sun, N.X.; Kalkur, T.S.; Sbrockey, N.M.; Tompa, G.S.; Guo, X.; Chen, C.-L.; Alpay, S.P.; Rosetti, G.A.; et al. Challenges and opportunities for multi-functional oxide thin films for voltage tunable RF/Microwave components. *J. Appl. Phys.* **2013**, *114*, 191301–191335.
2. Subramanyam, G.; Ahamed, F.; Biggers, R.; Neidhard, R.; Nykiel, E.; Ebel, J.; Strawser, R.; Stamper, K.; Calcatera, M. RF Performance evaluation of ferroelectric varactor shunt switches. *Microw. Opt. Technol. Lett.* **2005**, *47*, 370–374.
3. Jain, M.; Majumder, S.B.; Katiyar, R.S.; Agrawal, D.C.; Bhalla, A.S. Dielectric properties of sol–gel-derived MgO:$Ba_{0.5}Sr_{0.5}TiO_3$ thin-film composites. *Appl. Phys. Lett.* **2002**, *81*, 3212.
4. Saravanan, K.V.; Sudheendran, K.; Raju, K.C.J. Tunable dielectric characteristics of (111)-oriented barium strontium titanate thin films deposited on platinized Si substrates. *Electron. Mater. Lett.* **2012**, *8*, 571.
5. Jain, M.; Majumder, S.B.; Katiyar, R.S.; Bhalla, A.S. Novel barium strontium titanate $Ba_{0.5}Sr_{0.5}TiO_3$/MgO thin film composites for tunable microwave devices *Mater. Lett.* **2003**, *57*, 4232.
6. Petzelt, J.; Setter, N. Far infrared spectroscopy and origin of microwave losses in low loss ceramics. *Ferroelectrics* **1993**, *150*, 89–102.
7. Petzelt, J.; Kamba, S. Submillimeter and infrared response of microwave materials: Extrapolation to microwave properties. *Mater. Phys. Chem.* **2003**, *79*, 175–180.
8. Tagantsev, A.K.; Petzelt, J.; Setter, N. Relation between intrinsic microwave and submillimeter losses and permittivity in dielectrics. *Solid State Commun.* **1993**, *87*, 1117–1120.
9. Zurmuhlen, R.; Petzelt, J.; Kamba, S.; Voitsekhovskii, V.V.; Setter, N. Dielectric spectroscopy of $Ba(B'_{1/2}B''_{1/2})O_3$ complex perovskite ceramics: Correlation between ionic parameters and microwave dielectric properties. Part I—Infrared reflectivity study (10^{12}–10^{14} Hz). *J. Appl. Phys.* **1995**, *77*, 5341–5350.
10. Petzelt, J.; Kamba, S.; Kozlov, G.V.; Volkov, A.A. Dielectric properties of microwave ceramics investigated by far infrared and submillimeterwave spectroscopy. *Ferroelectrics* **1996**, *176*, 145–165.
11. Gevorgian, S. Ferroelectrics in Microwave Devices, Circuits and Systems. In *Chapter 2: Physics of the Tunable Ferroelectric Devices*; Springer: London, UK, 2009; pp. 21–59.
12. Kittel, C. *Introduction to Solid State Physics*, 5th ed.; John Wiley and Sons: Hoboken, NJ, USA, 1976; Chapter 13.
13. Hench, L.L.; West, J.K. *Principles of Electronic Ceramics*; John Wiley and Sons: Hoboken, NJ, USA, 1989; Chapter 6.
14. Rupprecht, G.; Bell, R.O. Dielectric Constant in Paraelectric Perovskites. *Phys. Rev.* **1964**, *135*, A748.
15. Hoshina, T.; Sase, R.; Nishiyama, J.; Takeda, H.; Tsurumi, T. Effect of oxygen vacancies on intrinsic dielectric permittivity of strontium titanate ceramics. *J. Cer. Soc. Jap.* **2018**, *126*, 263–268.
16. Cochard, C.; Spielmann, T.; Granzow, T. Dielectric tunability of ferroelectric barium titanate at millimeter-wave frequencies. *Phys. Rev. B* **2019**, *100*, 184104.
17. Ihlefeld, J.F.; Harris, D.T.; Keech, R.; Jones, J.L.; Maria, J.P.; Trolier-McKinstry, S. Scaling Effects in Perovskite Ferroelectrics: Fundamental Limits and Process-Structure-Property Relations. *J. Am. Ceram. Soc.* **2016**, *99*, 2537–2557.
18. Kay, H.F.; Vousdan, P. Symmetry changes in barium titanate at low temperatures and their relation to its ferroelectric properties. *Phil. Mag.* **1949**, *40*, 1019.
19. Zhang, Q.M.; Wang, H.; Kim, N.; Cross, L.E. Direct evaluation of domain-wall and intrinsic contributions to the dielectric and piezoelectric response and their temperature dependence on lead zirconate-titanate ceramics. *J. Appl. Phys.* **1994**, *75*, 454.
20. Tagantsev, A.K.; Sherman, V.O.; Astafiev, K.F.; Venkatesh, J.; Setter, N. Ferroelectric Materials for Microwave Tunable Applications. *J. Electroceramics* **2003**, *11*, 5–66.
21. Hashemizadeha, S.; Damjanovic, D. Nonlinear dynamics of polar regions in paraelectric phase of $(Ba_{1-x},Sr_x)TiO_3$ ceramics. *Appl. Phys. Lett.* **2017**, *110*, 192905.
22. Rusek, K.; Kruczek, J.; Szot, K.; Rytz, D.; Go'rny, M.; Roleder, K. Non-Linear Properties of $BaTiO_3$ above T_c. *Ferroelectrics* **2008**, *375*, 165.
23. Ko, J.-H.; Kim, T.; Roleder, K.; Rytz, D.; Kojima, S. Precursor dynamics in the ferroelectric phase transition of barium titanate single crystals studied by Brillouin light scattering. *Phys. Rev. B* **2011**, *84*, 094123.

24. Darlington, C.N.W.; Cernik, R.J. The ferroelectric phase transition in pure lightly doped barium titanate. *J. Phys. Condens. Matter* **1991**, *3*, 4555.
25. Garten, L.M.; Lam, P.; Harris, D.; Maria, J.P.; Trolier-McKinstry, S. Residual ferroelectricity in barium strontium titanate thin film tunable dielectrics. *J. Appl. Phys*. **2014**, *116*, 044104.
26. Uwe, H.; Yamaguchi, H.; Sakudo, T. Ferroelectric microregion in $KTa_{1-x}Nb_xO_3$ and $SrTiO_3$. *Ferroelectrics* **1989**, *96*, 123.
27. Biancoli, A.; Fancher, C.M.; Jones, J.L.; Damjanovic, D. Breaking of macroscopic centric symmetry in paraelectric phases of ferroelectric materials and implications for flexoelectricity. *Nat. Mater*. **2015**, *14*, 224.
28. Garten, L.M.; Trolier-McKinstry, S. Enhanced flexoelectricity through residual ferroelectricity in barium strontium titanate. *J. Appl. Phys*. **2015**, *117*, 094102.
29. Subramanyam, G.; Patterson, M.; Leedy, K.; Neidhard, R.; Varanasi, C.; Zhang, C.; Steinhauer, G. Linearity and temperature dependence of large area processed high Q BST varactors. *IEEE Trans. Ultrason. Ferroelectr. Freq. Control*. **2010**, *57*, 1692–1695.
30. Vailionis, A. The effects of strain on crystal structure and properties during epitaxial growth of oxides. In *Epitaxial Growth of Complex Metal Oxides*; Woodhead Publishing Series in Electronic and Optical Materials; Elsevier BV: Amsterdam, The Netherlands, 2015; pp. 175–207.
31. Choi, K.J.; Biegalski, M.; Li, Y.L.; Sharan, A.; Schubert, J.; Uecker, R.; Reiche, P.; Chen, Y.B.; Pan, X.Q.; Gopalan, V.; et al. Enhancement of ferroelectricity in strained $BaTiO_3$ thin films. *Science* **2004**, *306*, 1005–1009.
32. Haeni, J.H.; Irvin, P.; Chang, W.; Uecker, R.; Reiche, P.; Li, Y.L.; Choudhury, S.; Tian, W.; Hawley, M.E.; Craigo, B.; et al. Room-temperature ferroelectricity in strained $SrTiO_3$. *Nature* **2004**, *430*, 758–761.
33. Jia, C.L.; Mi, S.B.; Faley, M.; Poppe, U.; Schubert, J.; Urban, K. Oxygen octahedron reconstruction in the $SrTiO_3/LaAlO_3$ heterointerfaces investigated using aberration-corrected ultrahigh-resolution transmission electron microscopy. *Phys. Rev. B* **2009**, *79*, 081405R.
34. Schlom, D.G.; Chen, L.-Q.; Fennie, C.J.; Gopalan, V.; Muller, D.A.; Pan, X.; Ramesh, R.; Uecker, R. Elastic strain engineering of ferroic oxides. *MRS Bull.* **2014**, *39*, 118–130.
35. Pertsev, N.A.; Zembilgotov, A.G.; Tagantsev, A.K. Effect of mechanical boundary conditions on phase diagrams of epitaxial ferroelectric films. *Phys. Rev. Lett*. **1998**, *80*, 1988–1991.
36. Pertsev, N.A.; Zembilgotov, A.G.; Hoffman, S.; Waser, R.; Tagantsev, A.K. Ferroelectric thin films grown on tensile substrate: Renormalization of the Curie–Weiss law and apparent absence of ferroelectricity. *J. Appl. Phys*. **1999**, *85*, 1698.
37. Pertsev, N.A.; Tagantsev, A.K.; Setter, N. Phase transitions and strain-induced ferroelectricity in $SrTiO_3$ epitaxial thin films. *Phys. Rev. B* **2000**, *61*, R825–R829.
38. Pertsev, N.A.; Koukhar, V.G.; Waser, R.; Hoffman, S. Curie–Weiss type law for the strain and stress effects on the dielectric response of ferroelectric thin films. *Appl. Phys. Lett*. **2000**, *77*, 2596–2598.
39. Koukhar, V.G.; Pertsev, N.A. In-plane polarization states and their instabilities in polydomain epitaxial ferroelectric thin films. *Appl. Phys. Lett*. **2001**, *78*, 530.
40. Ban, Z.G.; Alpay, S.P. Phase diagrams and dielectric response of epitaxial barium strontium titanate films: A theoretical analysis. *J. Appl. Phys*. **2002**, *91*, 9288–9296.
41. Wang, Y.L.; Tagantsev, A.K.; Damjanovic, D.; Setter, N. Giant domain wall contribution to the dielectric susceptibility in $BaTiO_3$. *Appl. Phys. Lett.* **2007**, *91*, 062905.
42. Gu, Z.; Pandya, S.; Samanta, A.; Liu, S.; Xiao, G.; Myers, C.J.; Damodaran, A.R.; Barak, H.; Dasgupta, A.; Saremi, S.; et al. Resonant domain-wall enhanced tunable microwave dielectrics. *Nature* **2018**, *560*, 622.
43. Chang, W.; Gilmore, C.M.; Kim, W.J.; Pond, J.M.; Kirchoefer, S.W.; Qadri, S.B.; Chrisey, D.B.; Horwitz, J.S. Influence of strain on microwave dielectric properties of (Ba,Sr)TiO_3 thin films. *J. Appl. Phys.* **2000**, *87*, 3044.
44. Park, B.H.; Gim, Y.; Fan, Y.; Jia, Q.X.; Lu, P. High nonlinearity of $Ba_{0.6}Sr_{0.4}TiO_3$ films heteroepitaxially grown on MgO substrates. *Appl. Phys. Lett.* **2000**, *77*, 2587.
45. Li, H.; Roytburd, A.L.; Alpay, S.P.; Tran, T.D.; Salamanca-Riba, L.; Ramesh, R. Dependence of dielectric properties on internal stresses in epitaxial barium strontium titanate thin films. *Appl. Phys. Lett.* **2001**, *78*, 2354.
46. Ndiaye-Tandia, O.; Charles, M.; Allal, D.; Bocquet, B. A broadband electromagnetic characterization of $Ba_{0.7}Sr_{0.3}TiO_3$ thin films on coplanar waveguide up to microwave frequencies. In Proceedings of the 29th Conference on Precision Electromagnetic Measurements (CPEM 2014), Rio de Janeiro, Brazil, 24–29 August 2014; pp. 342–343.
47. Kim, T.-G.; Oh, J.; Kim, Y.; Moon, T.; Hong, K.S.; Park, B. Crystallinity Dependence of Microwave Dielectric Properties in (Ba,Sr)TiO_3 Thin Films. *Jpn. J. Appl. Phys.* **2003**, *42*, 1315.
48. Kim, H.-S.; Hyun, T.-S.; Kim, H.-G.; Kim, I.-D.; Yun, T.-S.; Lee, J.-C. Orientation effect on microwave dielectric properties of Si-integrated thin films for frequency agile devices. *Appl. Phys. Lett.* **2006**, *89*, 052902.
49. Simon, W.K.; Akdogan, E.K.; Safari, A.; Bellotti, J.A. In-plane microwave dielectric properties of paraelectric barium strontium titanate thin films with anisotropic epitaxy. *Appl. Phys. Lett.* **2005**, *87*, 082906.
50. Cole, M.W.; Weiss, C.V.; Ngo, E.; Hirsch, S.; Coryell, L.A.; Alpay, S.P. Microwave dielectric properties of graded barium strontium titanate films. *Appl. Phys. Lett.* **2008**, *92*, 182906.
51. Campbell, A.L.; Biggers, R.R.; Subramanyam, G.; Kozlowski, G.; Kleismit, R.A.; Zate, H.N.; Hopkins, S.C.; Glowacki, B.A.; Riehl, B.D.; Peterson, T.L. Microwave characterization of nanostructured ferroelectric $Ba_{0.6}Sr_{0.4}TiO_3$ thin films fabricated by pulsed laser deposition. *Nanotechnology* **2008**, *19*, 485704.

52. Kooriyattil, M.S.; Pavunny, S.P.; Instan, A.A.; Katiyar, R.S. The Thermal Stability of Voltage Tunability in Pulsed Laser Deposited $Ba_{0.6}Sr_{0.4}TiO_3$ Thin Films. *Integr. Ferroelectr.* **2015**, *166*, 140–149.
53. Chen, P.; Xu, S.Y.; Zhou, W.Z.; Ong, C.K. In situ reflection high-energy electron diffraction observation of epitaxial $LaNiO_3$ thin films. *J. Appl. Phys*. **1999**, *85*, 3000.
54. Subramanyam, G.; Heckman, E.; Grote, J.; Hopkins, F. Microwave dielectric properties of DNA based polymers between 10 and 30 GHz. *IEEE Microw. Wirel. Compon. Lett*. **2005**, *15*, 232–234.
55. Fompeyrine, J.; Berger, R.; Lang, H.P.; Perret, J.; Machler, E.; Gerber, C.; Locquet, J.-P. Local determination of the stacking sequence of layered materials. *Appl. Phys. Lett*. **1998**, *72*, 1697.
56. Guus, J.H.; Rijnders, G.; Koster, G.; Blank, D.H.A.; Rogalla, H. In situ monitoring during pulsed laser deposition of complex oxides using reflection high energy electron diffraction under high oxygen pressure. *Appl. Phys. Lett*. **1997**, *70*, 1888.
57. Zhu, J.; Li, Y.R.; Zhang, Y.; Liu, X.Z.; Tao, B.W. Effects of compressive and tensile stress on the growth mode of epitaxial oxide films. *Ceram. Int.* **2008**, *34*, 967–970.
58. Koster, G.; Huijben, M.; Janssen, A.; Rijnders, G. Growth studies of heteroepitaxial oxide thin films using reflection high-energy electron diffraction (RHEED). In *Epitaxial Growth of Complex Metal Oxides*; Woodhead Publishing Series in Electronic and Optical Materials; Elsevier BV: Amsterdam, The Netherlands, 2015; pp. 3–29.
59. Tang, F.; Parker, T.; Wang, G.-C.; Lu, T.-M. Surface texture evolution of polycrystalline and nanostructured films: RHEED surface pole figure analysis. *J. Phys. D Appl. Phys*. **2007**, *40*, R427–R439.
60. Vailionis, A.; Boschker, H.; Siemons, W.; Houwman, E.P.; Blank, D.H.A.; Rijnders, G.; Koster, G. Misfit Strain Accommodation in Epitaxial ABO3 Perovskites: Lattice Rotations and Lattice Modulations. *Phys. Rev. B* **2011**, *83*, 064101.
61. Tkach, A.; Okhay, O.; Reaneyb, I.M.; Vilarinho, P.M. Mechanical strain engineering of dielectric tunability in polycrystalline $SrTiO_3$ thin films. *J. Mater. Chem*. **2018**, *6*, 2467.
62. Perry, N.H.; Bishop, S.R.; Tuller, H.L. Tailoring chemical expansion by controlling charge localization: In situ X-ray diffraction and dilatometric study of $(La,Sr)(Ga,Ni)O_3$ perovskite. *J. Mater. Chem. A* **2014**, *2*, 18906.
63. Vélu, G.; Houzet, G.; Burgnies, L.; Carru, J.C.; Marteau, A.; Blary, K.; Lippens, D.; Mounaix, P.; Tondusson, M.; Nguéma, E. Electrical Characterizations of Paraelectric BST Thin Films up to 1 THz: Realization of Microwave Phase Shifters. *Integr. Ferroelectr.* **2007**, *93*, 110–118.
64. Matthews, J.W.; Blakeslee, A.E. Defects in epitaxial multilayers: III. Preparation of almost perfect multilayers. *J. Cryst. Growth* **1974**, *27*, 118.
65. Eckstein, J.N.; Zheng, M.; Zhai, X.; Davidson, B.; Warusawithana, M.; Oh, S. Chapter 21—Atomic layer-by-layer molecular beam epitaxy of complex oxide films and heterostructures. In *Molecular Beam Epitaxy: From Research to Mass Production*; Henini, M., Ed.; Elsevier Science and Technology: Amsterdam, The Netherlands, 2013; pp. 509–528.
66. Peng, L.S.; Xi, X.; Moeckly, B.H.; Alpay, S.P. Strain relaxation during in situ growth of $SrTiO_3$ thin films. *Appl. Phys. Lett*. **2003**, *83*, 4592.
67. Speck, J.S.; Pompe, W. Domain configurations due to multiple misfit relaxation mechanisms in epitaxial ferroelectric thin films. I. Theory. *J. Appl. Phys*. **1994**, *76*, 466.
68. Jesson, D.E.; Pennycook, S.J.; Baribeau, J.-M.; Houghton, D.C. Surface stress, morphological development, and dislocation nucleation during strained-layer epitaxy. *MRS Online Proc. Libr.* **1993**, *317*, 31–37.
69. Jesson, D.E.; Pennycook, S.J.; Baribeau, J.-M.; Houghton, D.C. Direct imaging of surface cusp evolution during strained-layer epitaxy and implications for strain relaxation. *Phys. Rev. Lett.* **1993**, *71*, 1744.
70. Chen, J.H.; Jia, C.L.; Urban, K.; Chen, C.L. Unusual lattice distortion in a $Ba_{0.5}Sr_{0.5}TiO_3$ thin film on a $LaAlO_3$ substrate. *Appl. Phys. Lett*. **2002**, *81*, 1291.
71. Tse, Y.Y.; Suherman, P.M.; Jackson, T.J.; Jones, I.P. Effect of growth defects on microwave properties in epitaxial $Ba_{0.5}Sr_{0.5}TiO_3$ thin films grown on (001) MgO by pulsed laser deposition. *Philos. Mag.* **2008**, *88*, 2505–2518.
72. Tagantsev, A.K.; Pertsev, N.A.; Muralt, P.; Setter, N. Strain-induced diffuse dielectric anomaly and critical point in perovskite ferroelectric thin films. *Phys. Rev. B* **2001**, *65*, 012104.
73. Oja, R.; Johnston, K.; Frantti, J.; Nieminen, R.M. Computational study of (111) epitaxially strained ferroelectric perovskites $BaTiO_3$ and $PbTiO_3$. *Phys. Rev. B* **2008**, *78*, 094102.
74. Ban, Z.-G.; Alpay, S.P. Optimization of the tunability of barium strontium titanate films via epitaxial stresses. *J. Appl. Phys*. **2003**, *93*, 504–511.
75. Shirokov, V.B.; Shakhovoy, R.A.; Razumnaya, A.G.; Yuzyuk, Y.I. Phenomenological theory of phase transitions in epitaxial $Ba_xSr_{1-x}TiO_3$ thin films on (111)-oriented cubic substrates. *J. Appl. Phys*. **2015**, *118*, 024101.
76. Wu, H.; Ma, X.; Zhang, Z.; Zeng, J.; Wang, J.; Chai, G. Effect of crystal orientation on the phase diagrams, dielectric and piezoelectric properties of epitaxial $BaTiO_3$ thin films. *AIP Adv.* **2016**, *6*, 015309.
77. Misirlioglu, I.B.; Akcay, G.; Alpay, S.P. Polarization Variations Due to Dislocation Configurations in Heteroepitaxial Ferroelectric Layers. *Integr. Ferroelectr.* **2006**, *83*, 67–80.
78. Catalan, G.; Sinnamon, L.J.; Gregg, J.M. The effect of flexoelectricity on the dielectric properties of inhomogeneously strained ferroelectric thin films. *J. Phys. Condens. Matter* **2004**, *16*, 2253.
79. Saad, M.M.; Baxter, P.; Bowman, R.M.; Gregg, J.M.; Morrison, F.D.; Scott, J.F. Intrinsic dielectric response in ferroelectric nanocapacitors. *J. Phys. Condens. Matter* **2004**, *16*, L451.

80. Arlt, G.; Böttger, U.; Witte, S. Dielectric dispersion of ferroelectric ceramics and single crystals at microwave frequencies. *Ann. Phys.* **1994**, *506*, 578–588.
81. Aschauer, U.; Pfenninger, R.; Selbach, S.M.; Grande, T.; Spaldin, N.A. Strain-controlled oxygen vacancy formation and ordering in $CaMnO_3$. *Phys. Rev. B Condens. Matter Mater. Phys.* **2013**, *88*, 054111.
82. Balzar, D.; Ramakrishnan, P.A.; Spagnol, P.D.; Mani, S. Influence of Strains and Defects on Ferroelectric and Dielectric Properties of Thin-Film Barium-Strontium Titanates. *Jpn. J. Appl. Phys.* **2002**, *41*, 6628–6632.
83. Yang, Q.; Cao, J.X.; Ma, Y.; Zhou, Y.C.; Jiang, L.M.; Zhong, X.L. Strain effects on formation and migration energies of oxygen vacancy in perovskite ferroelectrics: A first-principles study. *J. Appl. Phys.* **2013**, *113*, 184110.
84. Vendik, O.G.; Ter-Martirosyan, L.T.; Zubko, S.P. Microwave losses in incipient ferroelectrics as functions of the temperature and the biasing field. *J. Appl. Phys.* **1998**, *84*, 993–998.
85. Vendik, O.G.; Zubko, S.P.; Nikol'ski, M.A. Microwave loss-factor of $Ba_xSr_{1-x}TiO_3$ as a function of temperature, biasing field, barium concentration, and frequency. *J. Appl. Phys.* **2002**, *92*, 7448–7452.
86. Vendik, O.G. Ferroelectrics Find Their "Niche" among Microwave Control Devices. *Phys. Solid State* **2009**, *51*, 1529–1534.